Simultaneous determination of inclusion crystallography and nanotube conformation for a Sb_2O_3/single-walled nanotube composite

S. Friedrichs, J. Sloan,* and M. L. H. Green
Wolfson Catalysis Centre (Carbon Nanotechnology Group), Inorganic Chemistry Laboratory, South Parks Road, Oxford OX1 3QR, United Kingdom

J. L. Hutchison
Department of Materials, Parks Road, Oxford, OX1 3PH, United Kingdom

R. R. Meyer and A. I. Kirkland†
Department of Materials Science, Pembroke Street, Cambridge CB2 3QZ, United Kingdom
(Received 30 January 2001; published 29 June 2001)

We report the structural solution of a one-dimensional Sb_2O_3 crystal incorporated within a helical (21,-8) single-walled carbon nanotube. The structures of both the encapsulated crystal and nanotube have been quantified using the phase image recovered via a modified object wave restoration scheme.

DOI: 10.1103/PhysRevB.64.045406 PACS number(s): 61.48.+c, 07.05.Pj, 68.37.Lp, 61.46.+w

I. INTRODUCTION

We recently showed that a 3×3 atomic layer one-dimensional (1D) crystal of KI incorporated within a single-walled carbon nanotube (SWNT) could be characterized on an ''atom-by-atom'' basis from the phase image restored from a focal series of images.[1] In this previous example the crystal was imaged along the unit-cell diagonal (i.e., $\langle 110\rangle$) relative to the bulk KI structure, which meant that all the imaged atom columns consisted of either pure K or pure I.[2] In the restored phase image, the phase shift produced by each atom column and by the SWNT walls was proportional to the electron density in projection and it was possible, therefore, to determine the precise number and type of atoms in each column in a repeating sequence of 1I-2K-3I-2K-1I and 1K-2I-3K-2I-1K {100} layers formed along the SWNT axis. In addition, atom column positional shifts relative to the bulk structure were measured. These were attributed to local distortions imposed by a reduction in coordination for the surface atoms of the inclusion crystal and also to constraints imposed by the confining surface of the SWNT. In spite of this level of structural characterization, information regarding the structural conformation of the host SWNT was absent as atomic detail from the SWNT was not resolved. In the absence of such information, a complete *ab initio* determination of the physical properties of such a composite (and therefore subsequent experimental verification) is impossible.

In this paper we report the characterization of an encapsulated nanocrystal of Sb_2O_3 based on the valentinite structure in which the atomic thickness in projection of individual antimony columns has been determined. Within the nanocrystal there is evidence for both local structural distortion and a substantial overall lattice contraction of the crystal along the tube axis. A detailed analysis of asymmetric fringe contrast in the tube walls has provided strong evidence for the chiral conformation (including the handedness) of the nanotube itself. The conformation is determined simultaneously together with the inclusion crystallography.

II. EXPERIMENTAL

A. Synthesis and specimen preparation

SWNT's were produced using a metal catalyzed arc synthesis procedure similar to the method previously reported[3] and filled according to the capillary technique.[4] A ground mixture of as-prepared SWNT's (0.030 g) and Puratronic Sb_2O_3 (ALFA, 99.999%) (0.150 g) was sealed into a quartz ampoule, heated at 1 K min^{-1} to 1033 K, held at that temperature for 180 min, and then allowed to slowly cool to room temperature inside the furnace. The product was reground, dispersed in Analar pentane and placed dropwise onto a holey carbon support grid.

The product was examined at 300 kV in a Japan Electron Optics Laboratory (JEOL) JEM-3000F field emission gun transmission electron microscope (FEGTEM), with a spherical aberration coefficient (C_S) of 0.57 mm and a point resolution of 0.16 nm.[5] In order to confirm the composition of the filling material, energy dispersive x-ray microanalysis (EDX) spectra were recorded from discrete filled SWNT's with an Oxford Instruments ISIS 300 system equipped with a LINK ''Pentafet'' detector and utilizing a minimum 0.5-nm-diam probe. High resolution images of individual filled nanotubes were acquired at a magnification of $\times600\,000$ using a GATAN 794 (1 k$\times$1 k pixel) charge-coupled device (CCD) camera. The microscope alignment was corrected for axial coma and twofold astigmatism using power spectra obtained from amorphous regions of the carbon support film.[6] The direct magnification at the plane of the CCD camera was independently calibrated at a known objective lens current using Si {110} lattice fringes. For suitable nanotubes a focal series of 20 images was recorded at an exposure of 1 s with a nominal focal increment between each image of 11 nm together with a final image with the nominal starting defocus in order to assess the specimen drift and beam damage.

B. Image processing and simulation

From each series of images, the exit plane wavefunction was restored using a linear Wiener filter restoration algo-

rithm as described elsewhere.[7,8] In order to restore the exit plane wave function the aberrations in each image must be measured to high accuracy. In this work these were determined using the methods described previously,[9,10] which do not rely on the presence of significant amounts of amorphous material.

Initially the relative defocus value and displacement vector of each image relative to an arbitrary reference image chosen from within the series were determined using the phase-compensated phase correlation function (PCF), (1),

$$X_{\mathrm{PCF}}(\mathbf{r}) = F^{-1}\left[W(k)\,\mathrm{sgn}(\cos(\pi\lambda D k^2))\,\frac{f_1^*(\mathbf{k}) f_2(\mathbf{k})}{|f_1^*(\mathbf{k}) f_2(\mathbf{k})|}\right], \tag{1}$$

where $f_i(\mathbf{k})$ is the Fourier transform of image i and $W(k)$ is a real and positive weighting factor used to suppress the influence of very high spatial frequencies which in general only contribute noise to the PCF. The sign function (sgn) in Eq. (1) is a phase compensation factor which inverts the sign of the cross spectrum for appropriate spatial frequencies, such that at the correct compensated focus difference D the contributions of all frequencies are positive, leading to a pronounced maximum of the PCF peak height as a function of D. The displacement between the images is then given by the position of this PCF peak.

In comparison to a standard cross-correlation function (XCF), the contribution of each Fourier component is independent of its strength, so that the PCF is not dominated by strong low-frequency shading patterns or by crystal reflections that lead to unwanted periodic repetitions of the XCF peak for crystalline objects. After registration of two initial images with the reference image, the image wave in the reference image plane can be restored, and further images can be iteratively added. The accuracy in the registration of the additional images is improved by maximizing the PCF peak height calculated from the correlation between the image to be added with images predicted from the current restoration as a function of the predicted image defocus.

For regions of the image taken around the nanotube, however, the relative focus determination did not work reliably, presumably because the nanotube, suspended only at one end, rotated slightly between exposures. Therefore, the relative focus level determination was performed on a small adjacent region of amorphous carbon. Subsequently, the displacements and rotations for six small (200 pixel square) overlapping subregions along the tube axis were determined by maximizing the PCF peak height as a function of the rotation angle with the relative focus levels fixed. For each subregion, the image wave in the reference plane was restored using only 13 of the 20 images, since in the other images the tube had evidently twisted and tilted the crystal off axis as easily seen by a comparison with predicted images.

The absolute defocus and astigmatism were then determined for each subregion using the phase contrast index (PCI) function (2),[9,10]

$$f_{\mathrm{PCI}}(\mathbf{k}, C_1, A_1) = -\cos[\arg(\psi(\mathbf{k})) + \arg(\psi(-\mathbf{k})) + 2\gamma(\mathbf{k}, C_1, A_1)], \tag{2}$$

where ψ represents the restored image wave and γ is the wave aberration function with defocus C_1 and twofold astigmatism A_1 as parameters.[6] When the correction parameters C_1, A_1 match the actual aberration parameters, f_{PCI} will tend to be 1 (or at least positive when noise is present) for all spatial frequencies.

Using the aberrations thus determined, the object wave for each subregion can be restored using a Wiener filter which also corrects for the attenuation at high spatial frequencies due to the coherence envelopes, specimen vibration, and the modulation transfer function of the CCD detector.[11–13] However, the extent to which these attenuations can be corrected is ultimately limited by noise. The Wiener filter is designed to give an optimum estimate of the real-space wavefunction in the presence of noise and will yield an effective wave transfer function (T_w) from the object wave to the restored object wave that is uniform over a range of spatial frequencies and decays to zero for higher spatial frequencies, with the cutoff frequency being 6 nm^{-1} for this data. Furthermore, due to the lack of very low spatial frequency phase contrast in any image, the restored wave

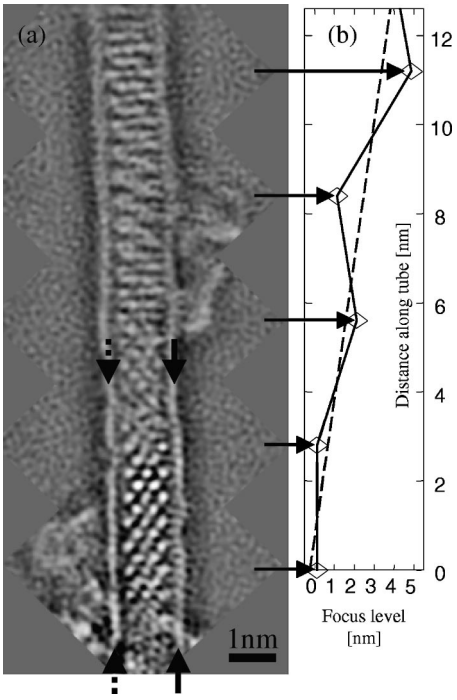

FIG. 1. (a) Phase image of the Sb_2O_3-filled carbon nanotube restored from a 20 member focal series. The image is composed of six individually restored overlapping subregions along the tube (uppermost subregion not shown). The lower part shows the crystal clearly resolved and also regular fringe contrast along the right tube wall. (b) The focus levels measured for the individual subregions show a systematic increase along the tube, indicating that it is inclined with respect to the image plane. The gradient of the straight line fitted to the six measured values (dashed) gives an estimate for the inclination angle.

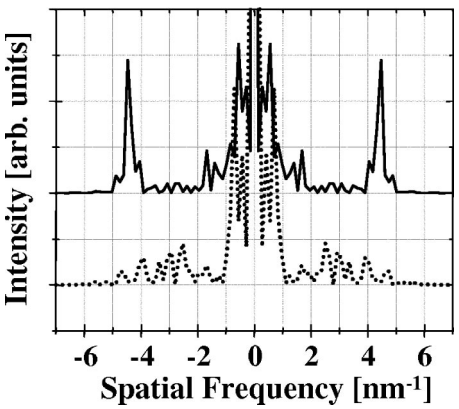

FIG. 2. Power spectra of one-dimensional line scans along the tube walls as indicated by arrows in Fig. 1(a). The spectrum for the right wall (solid graph) shows a strong peak corresponding to spacing of 0.224 nm. The peak is absent for the left wall (dotted graph), indicating that the tube is chiral and inclined to the image plane.

$\psi_{\mathrm{rest}}(\mathbf{k})$ also contains unwanted contributions from the conjugate object wave $\psi^*_{\mathrm{obj}}(-\mathbf{k})$. However, the corresponding conjugate wave transfer function (T_{cw}) is close to zero for all but the very low spatial frequencies.

The restored subregions were combined to give the final restoration of the complete nanotube [Fig. 1(a)] in the same orientation and position as in the reference image. Simulations were performed using a standard multislice algorithm[14,15] using code provided by Kirkland.[16] The resultant complex exit wave functions were backpropagated to the center plane of the specimen, which for weak objects is the plane of minimum amplitude contrast and hence the plane in which the experimental object wave is restored. To account for the limited transfer band in the restored wave, the simulated restored wave is subsequently computed according to Eq. (3),

$$\psi_{\mathrm{sim,rest}} = T_w(\mathbf{k})\,\psi_{\mathrm{sim,obj}}(\mathbf{k}) + T_{cw}(\mathbf{k})\,\psi^*_{\mathrm{sim,obj}}(-\mathbf{k}). \quad (3)$$

Atomic coordinates for (n,m) nanotubes were generated by mapping the strip $\{\mathbf{r}|0 \leqslant \mathbf{r}\cdot\mathbf{c}_h < |\mathbf{c}_h|^2\}$ of a planar hexagonal graphene lattice (with a carbon-carbon distance $d_{\mathrm{C\text{-}C}} = 0.144\,\mathrm{nm}$ and lattice vectors $\mathbf{a}_1, \mathbf{a}_2$) onto a cylinder surface (Fig. 3). The indices (n,m) with $n > 0$ and $-n/2 < m \leqslant n$ (Ref. 17) uniquely define the structure of the nanotube via the chiral vector $\mathbf{c}_h = n\mathbf{a}_1 + m\mathbf{a}_2$.[18] The special cases $(n,0)$ and (n,n) represent the nonchiral zigzag and armchair configurations, respectively, while all other nanotubes are chiral with $(n+m,-m)$ being the mirror image of (n,m). The coordinates for the encapsulated crystal were determined from a fragment generated from the valentinite form of Sb_2O_3.[19]

III. RESULTS AND DISCUSSION

A. The tube conformation

Figure 1(a) shows the restored phase image of a $(21,-8)$ SWNT containing an encapsulated single crystal of Sb_2O_3. The restoration is composed of six individually restored overlapping subregions. The plot [Fig. 1(b)] of the absolute focus values measured for these subregions shows a systematic increase of about 4 nm in the measured overfocus towards the top end of the tube. This indicates that the tube is inclined with respect to the image plane, with the top end in Fig. 1(a) higher in the beam path. Fitting a straight line to these values gives a standard deviation $\sigma_{n-2} = 1.1\,\mathrm{nm}$ for the six individual focus values and yields an inclination angle of $\beta = 17° \pm 5°$.

This is consistent with the observation that the right wall of the SWNT displays a periodic lattice spacings of $0.224 \pm 0.04\,\mathrm{nm}$, whereas the contrast variations on the left wall are effectively random, as confirmed by 1D power spectra obtained from single-pixel line traces along both tube walls (Fig. 2). The observed periodic spacing on the right wall corresponds to the center-to-center spacing $1.5 d_{\mathrm{C\text{-}C}} = 0.216\,\mathrm{nm}$ between neighboring ''zigzag'' rows of carbon atoms in the SWNT wall lattice when viewed in projection.

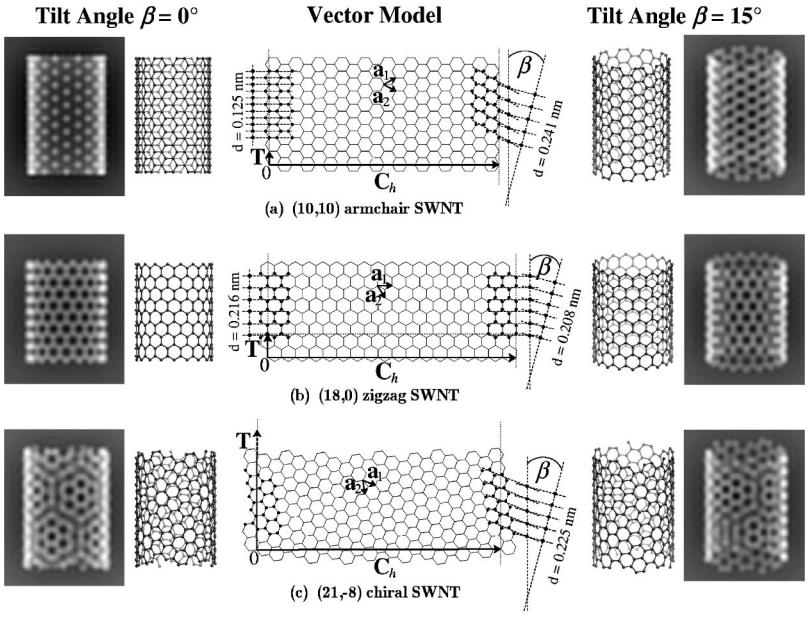

FIG. 3. Schematic illustration of the observable resolution of fringes along SWNT walls, depending on the conformation and the tilt angle β. The middle column shows the unrolled hexagonal graphene sheet, illustrating how the orientation of the chiral vector $\mathbf{C}_h$ with respect to the lattice vectors $\mathbf{a}_1$ and $\mathbf{a}_2$ defines the rolling of a strip of width $|\mathbf{C}_h|$ into a nanotube of a specific conformation and diameter. The columns adjacent to the illustrated graphene sheet display modeled fractions of the SWNT's, where the models on the right are tilted by $\beta = 15°$ out of the image plane. The outermost columns show simulated phase images of the displayed models.

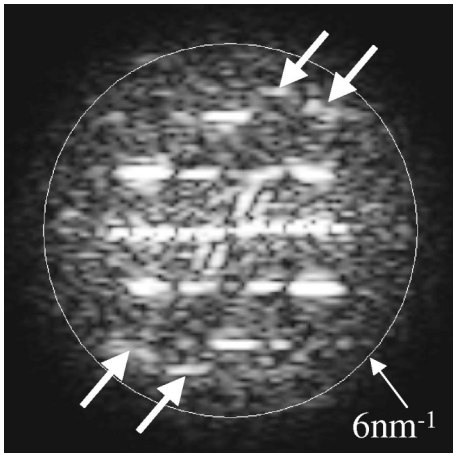

FIG. 4. Square root of the two-dimensional power spectrum of the tube in the lower half of Fig. 1(a). The reflections marked by arrows are incommensurate to the crystal reflections and arise from the tube itself.

The extent to which such spacings are visible is determined by the image resolution, the relative conformation of the nanotube, and also the tilt of the tube relative to the electron beam. In Fig. 3 the relationship between the observed wall periodicity, nanotube conformation, and tilt angle is illustrated with structure models and corresponding simulations of three SWNT's that closely match the experimental tube diameters of 1.4 nm. In case of achiral tubes [Figs. 3(a) and 3(b)] the observed contrast on both walls is always equal. In the case of an unrotated armchair tube [Fig. 3(a) left], no wall contrast would be observable, as the spacing of only 0.125 nm is beyond the experimental resolution. In the case of an unrotated ''zigzag'' tube [Fig. 3(b) left], both carbon walls are clearly visible as the zigzag lines have a separation of 0.216 nm in projection. As the tube is rotated, the simulated wall spacings smear as the carbon zigzags start to stagger in projection.

A chiral tube [e.g., Fig. 3(c)], however, will display resolvable contrast on the left (right) tube wall if the value of the difference $\delta=|\alpha-\beta|$ ($\delta=|\alpha+\beta|$) is small, where $\alpha=\angle(\mathbf{C}_h,\mathbf{a}_1)=\arctan[\sqrt{3}m/(2n+m)]$ is the chiral angle and the angle β between the tube axis and the image plane is defined as positive if the top end of the tube is above the image plane (as for this specimen). The observed contrast on the right wall of the imaged tube in Fig. 1(a) therefore means that the tube is chiral with a negative chiral angle α and hence a negative integer m. As the number of atoms in projection on the tube wall is small, strong contrast will be visible for values for δ of up to 10°, and the observed spacing is given by $1.5d_{\text{C-C}}\cos\beta/\cos\alpha$ as illustrated with the lattice model for $\mathbf{C}_h=(21,-8)$ in Fig. 3(c).

Further information on the tube chirality can be obtained from the Fourier transform of the restored wave. The spots marked by arrows in Fig. 4 are not commensurate with the reflections due to the encapsulated crystal. A further confirmation that these spots arise from the nanotube itself is that the k_y component of the more intense spots corresponds to the spacing observed in the line scan along the right tube wall. In order to determine the tube conformation multislice simulations for all tubes with diameters d in the range $0.137\,\text{nm}\leqslant d\leqslant 0.150\,\text{nm}$, tilted by angles of 0°, 5°, 10°, 15°, and 20° were calculated. The only tubes with negative chirality that reproduced the observed peaks in the power spectrum were (20, −7), (20, −6), and (21, −8) with tilt angles of 15° and 20°. As the diameter of the (21, −8) tube [which is the mirror image of a (13, 8) tube] provided the best match to the experimental diameter, this tube was used for all subsequent simulations. The simulated power spectra in Fig. 5 demonstrate how the positions of the first-order peaks depend on the chiral angle of the tube.

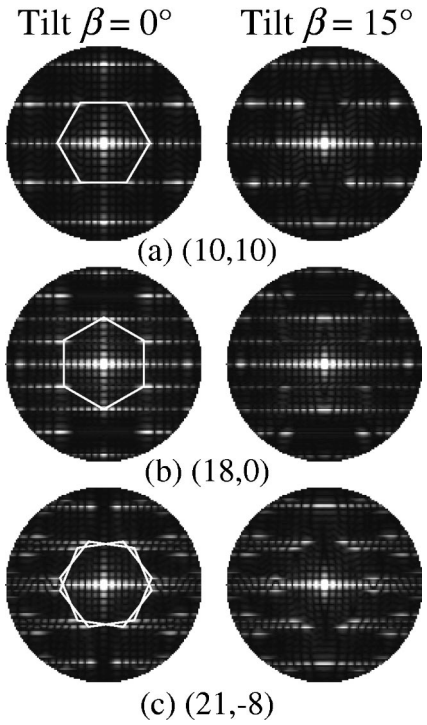

FIG. 5. Simulated object wave power spectra for (a) armchair, (b) zigzag, and (c) chiral tube conformations. The first-order reflections are situated on the vertices of two hexagons (due to the contributions from the upper and lower tube wall, respectively) which are rotated by $\pm\alpha$ with respect to the tube axis. In case of the achiral armchair (a) and zigzag (b) conformations, both hexagons coincide. In all figures, the maximum spatial frequency shown is 10 nm^{-1}.

B. The encapsulated crystal

The restored phase shows some contrast due to the filling material in the SWNT over the entire field of view. However, only within the lower region of the tube is the crystalline Sb_2O_3 sufficiently well resolved to provide useful structural information. Figure 6 shows the phase of this subregion with frequencies greater than the furthest crystal reflections filtered to reduce unnecessary high-frequency noise. The uninterpretable crystalline contrast in the remainder of the tube is in part due to movement and rotation of the tube during data acquisition and to misorientation of the filling in some regions of the tube.

The white spots in the restored phase correspond to projections through atomic columns of antimony only. Due to

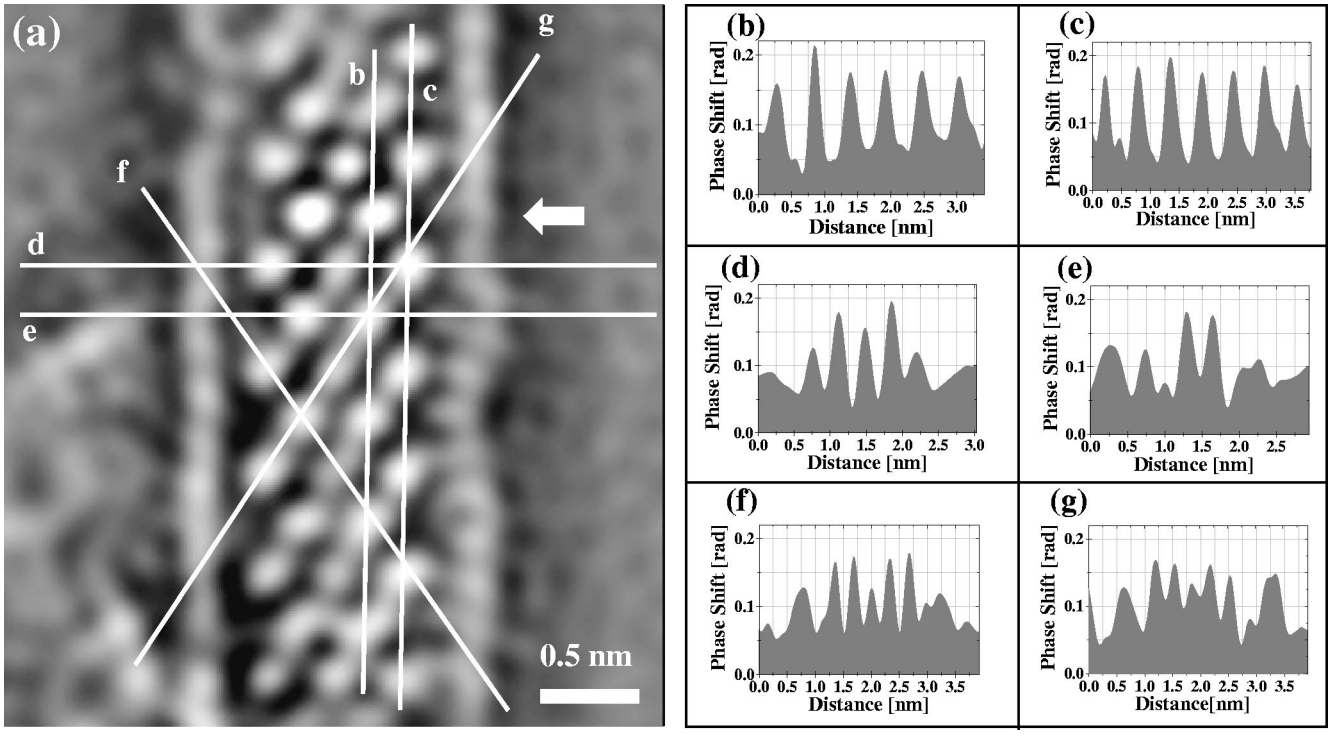

FIG. 6. (a) Noise-filtered detail of the phase image (Fig. 1), showing a projection close to $\langle 10\bar{1}\rangle$ of the encapsulated Sb_2O_3 crystal. The white arrow indicates a row of the crystal that is thought to consist of two four-member antimony columns, whereas all the other columns consist of two or three antimony atoms. (b)–(g) Single pixel line profiles obtained from line traces marked by the white lines in (a).

the weak scattering and staggering in projection of the oxygen positions and, additionally, the limited resolution (ca. 0.16 nm) present in the restoration, the oxygen sublattice could not be resolved. A comparison of multislice simulations of the restored phase of Sb_2O_3 lattice fractions of appropriate thickness with equivalent simulated antimony sublattice fractions confirmed that the phase contrast due to the oxygen sublattice is negligible compared to that due to the antimony sublattice.

The regular structural motif of the encapsulated Sb_2O_3 crystal can be described as a repeating sequence of a row containing three columns of antimony atoms followed by a row containing two columns of antimony atoms arranged perpendicular to the long axis of the tube. Within each three- or two-member row, the intensities of the peaks corresponding to individual antimony columns vary in a complex fashion. The line profile across a three-member row [Fig. 6(d)] shows a stacking pattern of 3-2-3 antimony atoms in projection. By contrast the line profile across a two-member row [Fig. 6(e)] gives two peaks of equal intensity approximately equivalent to the higher peak within the three-member row indicating antimony columns of three atoms in thickness.

The phase image and corresponding line profiles in Fig. 6 can best be matched to an approximate $\langle 10\bar{1}\rangle$ projection through a fragment of Sb_2O_3 derived from the orthorhombic polymorph valentinite form, which consists of infinite double chains of Sb_2O_3 units [considered to be the high-pressure form of Sb_2O_3 (Ref. 19)], as opposed to the cubic senarmonite form, which consists of molecular units of Sb_4O_6.[20] In the bulk valentinite structure, the Sb_2O_3 double chains run parallel to $\langle 001\rangle$ with the two chains linked at each antimony site by a shared oxygen, such that each antimony atom is coordinated by three oxygen atoms.[19]

The proposed structure model and an end-on view of the Sb_2O_3/SWNT composite are shown in Figs. 7(a1) and 7 (a2). In this model, the tube axis is aligned with the $\langle 4\bar{1}2\rangle$ direction of the crystal, as this was the only possible tube axis that reproduced the good alignment of antimony atomic columns along the center line of the tube and was consistent with the observed tube tilt angle. The angle between $\langle 4\bar{1}2\rangle$ and the optimum $\langle 10\bar{1}\rangle$ viewing direction is 78.3°. Small deviations from this viewing direction make an insignificant difference to the observed contrast and hence a tube inclination of 15° (rather than 11.7°), as used in the right-hand side simulations in Fig. 3 and again in Fig. 7 in order to account for the observed contrast within the tube wall, is plausible.

Since the oxygen sublattice could not be resolved, the oxygen coordination in the model is as predicted from the bulk valentinite structure. In order to fit the modeled Sb_2O_3 crystal into the 1.45-nm-diam SWNT, some oxygen atoms on the surface of the crystal were omitted. This can be justified in terms of the reduction in coordination that will be expected at the Sb_2O_3/SWNT interface [cf. 2×2 and 3×3 KI crystals formed within SWNT's (Refs. 1 and 21)].

Figure 7(a3) shows the calculated multislice phase image of the structural model. Line profiles of this simulated phase image are shown in Figs. 7(b)–7(g). Comparison of the corresponding experimental line profiles in Figs. 6(b)–6(g) supports our interpretation of the phase image from the relative

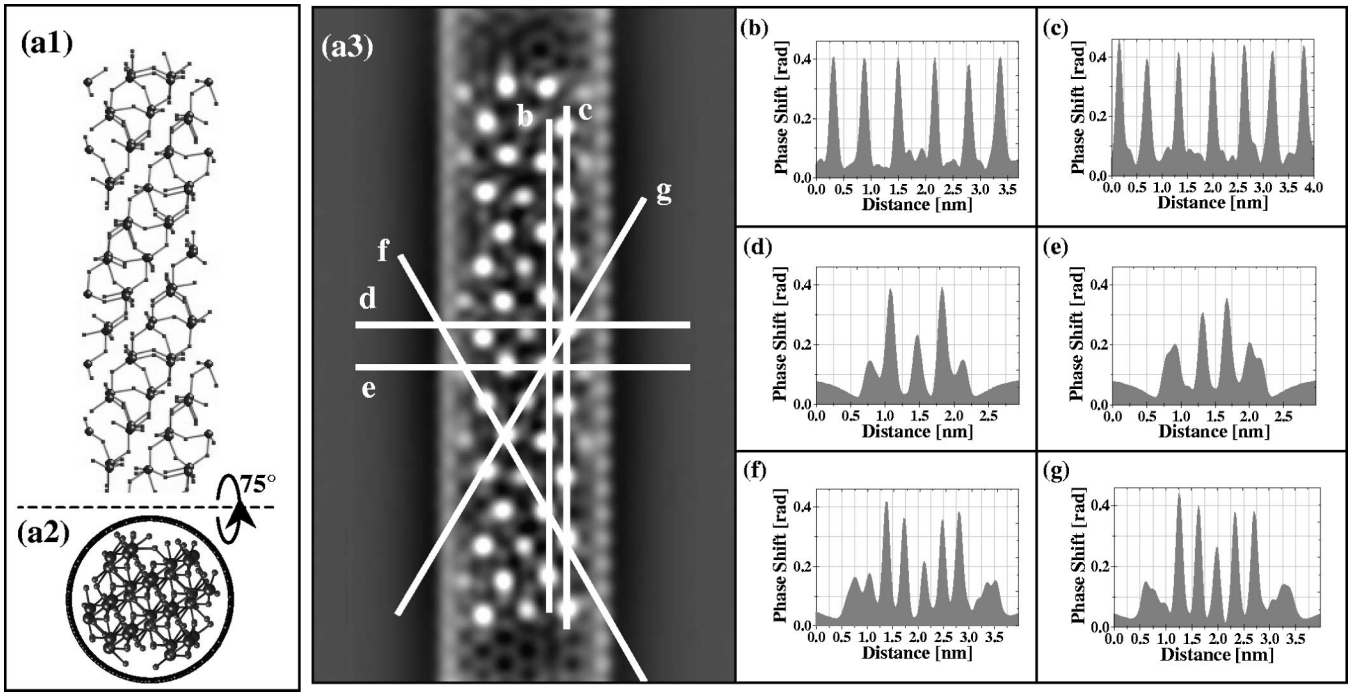

FIG. 7. (a1) Ball and stick model of the valentinite Sb_2O_3 crystal fraction as observed in the experimental viewing direction 3° off the $\langle 10\bar{1}\rangle$ projection. The antinomy atoms are represented by the larger balls. (a2) View along the tube axis of the (21, −8) SWNT, which is parallel to the $\langle 4\bar{1}2\rangle$ direction of the encapsulated Sb_2O_3 crystal. (a3) Simulated restored phase for this composite Sb_2O_3/SWNT model. (b)–(g) Single pixel line profiles obtained from line traces marked by the white lines in (a3).

intensities of the peaks in the line profiles although we note that the absolute intensities of the phase shifts are about twice as high as the experimental phase shifts. This discrepancy between the contrast of simulated and experimental conventional high-resolution TEM (HRTEM) images has been observed before but remains relatively poorly understood.[22]

The simulation in Fig. 7(a3) also shows weak contrast close to the tube walls and corresponding to the single atom columns at the edge of the encapsulated valentinite crystal fragment. The corresponding experimental phase also shows some evidence for additional weak peaks at certain of these sites, possibly corresponding to individual antimony atoms. However, the intensities of these peaks are sufficiently close to the background noise levels that it is impossible to definitely assign these to such columns without a more accurate analysis of the phase contrast.

Within the nanocrystal there is also some evidence for local structural irregularity. The two-atom row marked with an arrow in Fig. 6(a3) gives a line profile with a peak height 30% greater than the equivalent peak height from the other two-atom rows [such as that marked by line (e) corresponding to the profile in Fig. 6(e)]. This observation is confirmed by the increased height of the second peak in the line profile Fig. 6(b). Together these line profiles suggest a possible antimony stacking arrangement of 4-4 atomic layers in the particular row marked with the arrow. In a similar fashion the center row of the crystal (i.e., parallel to the tube axis) consists of columns mostly containing just two antimony atoms. This was also assumed in the structural model in Fig. 7(a1). However, there is evidence from increased peak heights in the line profiles that some of these equivalent columns contain three atoms, especially at sites close to the indicated 4-4 row. The end-on view [Fig. 7(a2)] of the model shows that a third antimony atom could easily be accommodated within the (21,−8) SWNT in the voids above and below the two-member antimony columns.

Significant lattice distortions were observed in the Sb_2O_3. In comparison with the bulk structure of valentinite, the encapsulated crystal shows a longitudinal contraction of 13% along the $\langle 4\bar{1}2\rangle$ direction (i.e., along the tube axis). This contraction occurs in a similar fashion but is larger than that which we reported for the SWNT encapsulated KI 3×3 crystal.[1] Direct lattice measurements from the line traces given in Figs. 6(b) and 6(c) show an average spacing of ≈0.543 nm between two 3-2-3 rows, whereas in the simulated phase image (based on the bulk antimony positions) equivalent rows are spaced at average intervals of ≈0.625 nm. The observed lattice contraction may be caused by an interaction between the Sb_2O_3 crystal and the SWNT walls or may be partially caused by the reduction in coordination at the Sb_2O_3/SWNT interface.

Figure 8 shows the power spectrum of the simulated object wave for the enclosed crystal without the surrounding tube. It is apparent that each reflection has pronounced satellites, which arise due to the large pseudo-unit-cell of the crystal with a much shorter approximate repeat within the cell [i.e., along the tube axis, the structure repeats itself exactly only after four pairs of rows, cf. Fig. 7(a1)]. The satellite reflections are absent in the experimental power spectrum in Fig. 4, indicating that the crystal is forced into a state of higher symmetry due to the confinement by the tube walls.

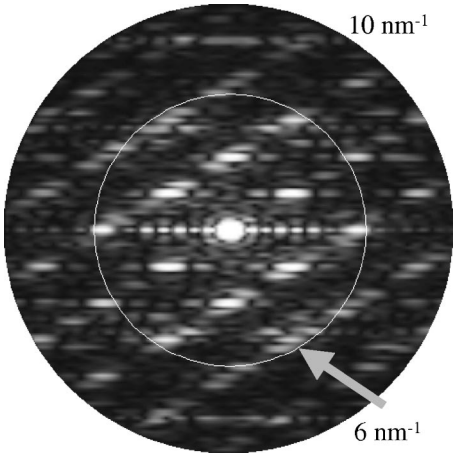

FIG. 8. Object wave power spectrum of the Sb_2O_3 crystal fraction model shown in Fig. 7 without the surrounding nanotube. The satellite reflections accompanying each peak are absent in the experimental power spectrum (Fig. 4), indicating that the crystal is forced into a state of higher symmetry.

IV. CONCLUSIONS

We have demonstrated a detailed structural characterization of a SWNT with an encapsulated Sb_2O_3 nanocrystal using the high resolution phase recovered from a focal series of images. As a consequence the following structural points emerge.

(1) The object wave restored from a focal series allowed a characterization of both the SWNT and the encapsulated crystal with an accuracy that could not be achieved from a single HRTEM image.

(2) The chiral tube conformation could be inferred from the measured tube diameter and from peak positions in the power spectrum of the restored wave, whereas previous studies of atomically resolved carbon SWNT's (Refs. 23 and 24) and subsequently boron nitride SWNT's (Ref. 25) applied to achiral tubes only.

(3) The chiral sense of a carbon nanotube has been directly determined using HRTEM. This has been achieved by an analysis of the asymmetric tube wall fringe contrast in combination with an accurate measurement of the change in defocus along the tube.

(4) The encapsulated crystal is based on a modified form of valentinite with significant lattice distortion parallel to the tube axis and with a higher crystal symmetry.

(5) Within the nanocrystal there is also evidence for local structural irregularity in the form of locally enhanced atom sites.

(6) At certain antimony sites near the tube wall there is a suggestion of single atom stacking.

(7) Although SWNT tube conformation has been determined by electron-diffraction studies,[24,26] scanning tunneling microscopy,[27] and by conventional HRTEM,[23–25] and the arrangement of a filling material has been investigated by high angle annular dark-field imaging in a scanning transmission electron microscope (STEM),[28] to the best of our knowledge this is the first time that SWNT conformation and detailed inclusion crystallography have been determined simultaneously.

ACKNOWLEDGMENTS

We acknowledge the Petroleum Research Fund, administered by the American Chemical Society (Grant No. 33765-AC5), the EPSRC (Grant Nos. GR/L59238, GR/L22324, GR/L10680, and GR/N17577) and Colebrand Ltd. for financial support. S.F. is indebted to BMBF and Fonds der Chemischen Industrie for additional financial support. J.S. is indebted to the Royal Society.

*Electronic address: jeremy.sloan@chemistry.oxford.ac.uk
†Electronic address: aik10@cam.ac.uk

[1] R. R. Meyer, J. Sloan, R. E. Dunin-Borkowski, A. I. Kirkland, M. C. Novotny, S. R. Bailey, J. L. Hutchison, and M. L. H. Green, Science **289**, 1324 (2000).

[2] If the K and I atoms are superposed in projection as in the case of a crystal viewed along ⟨100⟩, for example, then the resulting image contrast from both columns is summed in projection as we reported in Ref. 21 for a 2×2 KI crystal formed inside a SWNT.

[3] C. Journet, W. K. Maser, P. Bernier, A. Loiseau, M. Lamy de la Chapelle, S. Lefrant, P. Deniard, R. Lee, and J. E. Fischer, Nature (London) **388**, 756 (1997).

[4] J. Sloan, D. M. Wright, H. G. Woo, S. Bailey, G. Brown, A. P. E. York, K. S. Coleman, J. L. Hutchison, and M. L. H. Green, Chem. Commun. (Cambridge) **8**, 699 (1999).

[5] J. L. Hutchison, R. C. Doole, R. E. Dunin-Borkowski, J. Sloan, and M. L. H. Green, JEOL News, Electron Opt. Instrum. **34E**, 10 (1999).

[6] W. O. Saxton, J. Microsc. **179**, 201 (1995).

[7] W. O. Saxton, Scanning Microsc. Suppl. **2**, 213 (1988).

[8] A. I. Kirkland, W. O. Saxton, K. L. Chau, K. Tsuno, and M. Kawasaki, Ultramicroscopy **57**, 355 (1995).

[9] R. R. Meyer, A. I. Kirkland, and W. O. Saxton, Inst. Phys. Conf. Ser. **161**, 295 (1999).

[10] R. R. Meyer, A. I. Kirkland, and W. O. Saxton, Ultramicroscopy (to be published).

[11] R. R. Meyer and A. I. Kirkland, Microsc. Res. Tech. **49**, 269 (2000).

[12] R. R. Meyer, A. I. Kirkland, R. E. Dunin-Borkowski, and J. L. Hutchison, Ultramicroscopy **85**, 9 (2000).

[13] R. R. Meyer and A. Kirkland, Ultramicroscopy **75**, 23 (1998).

[14] J. M. Cowley and A. F. Moodie, Acta Crystallogr. **10**, 609 (1957).

[15] P. Goodman and A. F. Moodie, Acta Crystallogr., Sect. A: Cryst. Phys., Diffr., Theor. Gen. Crystallogr. **30**, 280 (1974).

[16] E. Kirkland, *Advanced Computing in Electron Microscopy* (Plenum Press, New York, 1998).

[17] The lower limit for m here differs from the definition given in Ref. 18 and ensures that the chiral angle α lies in the range $-30°<\alpha\leqslant30°$.

[18] R. Saito, G. Dresselhaus, and M. Dresselhaus, *Physical Properties of Carbon Nanotubes* (Imperial College Press, London, 1998).

[19] C. Svensson, Acta Crystallogr., Sect. B: Struct. Crystallogr. Cryst. Chem. **30**, 458 (1974).
[20] C. Svensson, Acta Crystallogr., Sect. B: Struct. Crystallogr. Cryst. Chem. **31**, 2016 (1975).
[21] J. Sloan, M. C. Novotny, S. R. Bailey, G. Brown, C. Xu, V. C. Williams, S. Friedrichs, E. Flahaut, R. L. Callender, A. P. E. York, K. S. Coleman, M. L. H. Green, R. E. Dunin-Borkowski, and J. L. Hutchison, Chem. Phys. Lett. **329**, 61 (2000).
[22] C. B. Boothroyd, J. Microsc. **190**, 99 (1998).
[23] D. Golberg, Y. Bando, L. Bourgeois, and K. Kurashima, Carbon **37**, 1858 (1999).
[24] P. Lambin, V. Meunier, L. Henrard, and A. A. Lucas, Carbon **38**, 1713 (2000).
[25] D. Golberg, Y. Bando, L. Bourgeois, K. Kurashima, and T. Sato, Appl. Phys. Lett. **77**, 1979 (2000).
[26] J. M. Cowley, P. Nikolaev, A. Thess, and R. E. Smalley, Chem. Phys. Lett. **265**, 379 (1997).
[27] J. W. G. Wildoer, L. C. Venema, A. G. Rinzler, R. E. Smalley, and C. Dekker, Nature (London) **391**(6662), 59 (1998).
[28] X. Fan, E. C. Dickey, P. C. Eklund, K. A. Williams, L. Grigorian, R. Buczko, S. T. Pantelides, and S. J. Pennycook, Phys. Rev. Lett. **84**, 4621 (2000).